IOP Publishing Semiconductor Science and Technology
Semicond. Sci. Technol. 32 (2017) 094002 (11pp) https://doi.org/10.1088/1361-6641/aa7ce6

Electrical modulation of weak-antilocalization and spin–orbit interaction in dual gated Ge/Si core/shell nanowires

R Wang[1], R S Deacon[1,2], J Yao[3], C M Lieber[3,4] and K Ishibashi[1,2]

[1] Advanced Device Laboratory, RIKEN, Wako, Saitama 351-0198, Japan
[2] Center for Emergent Matter Science (CEMS), RIKEN, Wako, Saitama 351-0198, Japan
[3] Deparment of Chemistry and Chemical Biology, Harvard University, Cambridge, MA 02138, United States of America
[4] School of Engineering and Applied Sciences, Harvard University, Cambridge, MA 02138, United States of America

E-mail: russell@riken.jp

Received 7 May 2017, revised 20 June 2017
Accepted for publication 30 June 2017
Published 9 August 2017

Abstract

Magnetic transport of holes in Ge/Si core/shell nanowires (NWs) is investigated under the control of dual electrical gating. The strength of the spin–orbit interaction (SOI) is analyzed from the weak-antilocalization (WAL) of the magnetoconductance (MC) as a function of a perpendicular magnetic field. By superimposing a small alternating signal on the voltage offset of both gates the universal conductance fluctuations are largely removed from the averaged MC traces, enabling a good fitting to WAL theory models. The tuning of both spin lifetime and the SOI strength is observed in the NWs with dual gating while the carrier density is kept constant. We observe an enhancement of spin lifetime with the mean free path due to the effect of geometrical confinement. The measured SOI energy of 1–6 meV may arise from the dipole coupled Rashba SOI, which is predicted to be one order of magnitude larger than the conventional Rashba coefficient in the Ge/Si core/shell NW system. A clear electrostatic modulation of SOI strength by a factor of up to three implies that Ge/Si NWs are a promising platform for the study of helical states, Majorana fermions and spin–orbit qubits.

Keywords: spin–orbit interaction, weak-antilocalization, nanowire

(Some figures may appear in colour only in the online journal)

Introduction

The effect of spin–orbit interaction (SOI) in materials without inversion symmetry splits the energy bands. Even in the absence of an external magnetic field, carriers coupled to the so-called spin–orbit effective field experience a resonant spin precession during ballistic travel [1, 2]. The SOI strength E_{SO} determines the speed of the spin rotation (or the spin–orbit length over which the spin undergoes a coherent rotation of π). Strong SOI is a key ingredient for the realization of Majarona states in semiconductor materials hybridized with s-wave superconductors [3–6]. Moreover, spin–orbit coupling enables spin manipulation by all electric means [7–10], which eases the device architecture and operation of spin transistors or spin–orbit qubits. The SOI in crystals may arise from the lattice inversion asymmetry known as Dresslhaus effect [11], or Rashba type structural symmetry breaking by unbalanced confinement potential or external electric field bias [12]. In the latter case the SOI strength (or the Rashba coefficient α) is proportional to the electrostatic field, opening a useful external tunable parameter to control the spin states and splitting energy.

Group IV Ge/Si core/shell NWs possess several unique features. A large valance band (VB) offset ~0.5 eV between Ge and Si naturally accumulates holes in the Ge core and forms a strong confinement field at the interface with the Si shell [13, 14]. Both Ge and Si are grown without dopants, ensuring high mobility with mean free paths up to ~500 nm

previously reported [13]. The quasi-1D Ge/Si NWs are easily segmented into zero-dimensional (0D) QDs by local electrical gates with energy level separations of a few meV [15, 16]. Kloeffel *et al* predicted a dipole coupled Rashba type SOI (DRSOI) in Ge/Si NWs due to the coexistence of the quasi-degeneracy of light and heavy holes close to the ground state and strong spin–orbit coupling of the atomic hole levels [17]. The DRSOI exhibits the same form as the normal Rashba SOI, in that both are linearly proportional to the electric field (E) across the nanowire. However, the underlying physics are different. Briefly, the transverse E-field across the nanowires will directly coupled to the spins when the hole wave functions are altered through the electric–dipole coupling. Such direct dipolar coupling SOI appears in the first order of the multiband perturbation theory and scales linearly with the radius (R) of the nanowires. The normal Rashba SOI for holes is a third order effect for which the spin splitting energy shrinks with increasing band gap (is inversely proportional to R). The DRSOI is expected to be sensitive to an external electrical field with a direct Rashba coefficient that is one or two orders larger than the conventional Rashba constant by a factor of $\sim R^2$ nm^{-2}, where $R = 5$–10 nm is the typical radius of the Ge/Si core/shell NWs. The DRSOI may give rise to a few meV spin splitting of the energy band under a moderate electric field with normal electrical gating. In addition, the Ge and Si both lack nuclear spin making the system attractive for the realization of spin qubits. The absence of hyperfine interaction prolongs the spin decoherence time, which is one vital bottleneck to limit the practical applications of Group III–V spin information quantum devices [7–10].

The SOI strength can be analyzed from the beat pattern of Shubnikov–de Haas oscillations in 2D systems [18, 19] or from the magnetic field dependent excited states spectroscopy of the 0D quantum dots [20–22]. A typical method to extract the SOI strength in 1D extended NWs is through the magnetoconductance (MC) measurements. In the presence (absence) of SOI, the quantum interference of the carrier wave functions will lead to a destructive (constructive) backscattering of the time-reversed trajectory pairs induced by scattering from randomly located impurities. An increase or decrease of conductance at zero magnetic field which is suppressed with increasing field is known as weak-antilocalization (WAL) and weak-localization (WL) respectively [23]. The strength of SOI in InAs and InSb wires has been extracted from WAL and is found to be a few hundreds μeV [24–28]. An electrostatic field control of the SOI strength has been achieved with dual gating on InAs NWs, revealing a tunable conventional Rashba effect [26, 27]. A couple of recent works have estimated the strength of SOI (with results comparable to reports for InSb NWs) in the Ge/Si NWs with either statistical analysis of Coulomb peak distributions [29] or WAL measurements [29, 30]. In these studies, the SOI was investigated in devices where one global gate controlled the carrier density and electric field across the NWs, simultaneously. The change of carrier density always alters the electron relaxation rate and hence affects the WAL features [26–28, 30]. To obtain an insight into the electric field modulation of the SOI in Ge/Si NWs and extract the Rashba coefficient, a dual gating configuration is necessary to maintain constant carrier density.

Here we present a study of magnetic transport in Ge/Si core/shell NWs under the control of dual electrical gating. The carrier density and electrical field inside the Ge/Si core/shell NWs are independently controlled by a top (TG) and back gate (BG) configuration. The SOI in the NWs is evaluated from fitting of the WAL observed in MC traces. The electric field across the wire modulates both the mean free path and the SOI strength. Larger mean free path is observed when holes are confined close to the NW center and leads to longer spin lifetime due to the cancellation of spin precession in a confined geometry. We expect that the relaxation rate will be dramatically suppressed in clean (or ballistic) devices, enabling the coherent spin evolution for spintronic applications. We find that for a large range of carrier density the SOI energy of Ge/Si NWs varies in a range of 1–6 meV, which is almost one order larger than the reported values of InSb or InAs NWs [24–28]. The SOI energy is tuned by a factor of up to three with electrostatic field. The corresponding Rashba coefficient is evaluated as $\sim$5 nm^2, much larger than the conventional Rashba constant of $\sim$0.4 nm^2 [17]. These results support the theoretical prediction of the existence of a strong DRSOI in Ge/Si core/shell NWs.

Results

Epitaxial Ge/Si core/shell NWs were synthesized by a two-step vapor–liquid–solid method and subsequently transferred onto target substrates using a home-made mechanical manipulator with micrometer precision. The growth and transfer of NWs have been described elsewhere (also see Methods) [31–34]. Figure 1(a) shows a schematic illustrating the architecture of the measured devices. The Ge/Si NW was placed on predefined bottom gates comprised of a Ti/Au BG for the transport channel and separated contact gates (CG). A 5 nm thin HfO_2 high-κ dielectric layer grown by atomic layer deposition (ALD) covered all the bottom gates. Electron beam evaporated 4-terminal Ti/Pd leads were used to contact the NW after a 3 s buffered hydrofluoric (BHF) etch to strip surface oxide and ensure good contact. An additional 5 nm HfO_2 ALD top layer was then grown at 80 °C on the NW followed with the deposition of a top gate (TG) covering the transport channel segment of the NW. The ultrathin high-κ dielectric layer enables an efficient gate capacitive coupling to tune the carrier density over a wide range. Moreover, the geometrical capacitance (C_g) of the thin high-κ dielectric film is comparable to the quantum capacitance (C_Q) of the wire allowing a portion of the voltage applied from the gates to drop across the NW, which leads to a band bending (or built-in electric field) inside the NWs.

Figure 1(b) shows a false color scanning electron microscopic image of a typical Ge/Si core/shell NW device. In the present study, electrical and magnetic transport was studied in three devices with different channel length (L) of 1 μm, 2 μm and 5 μm, respectively. The magnetic (B) field was applied perpendicular to the NW and substrate surface.

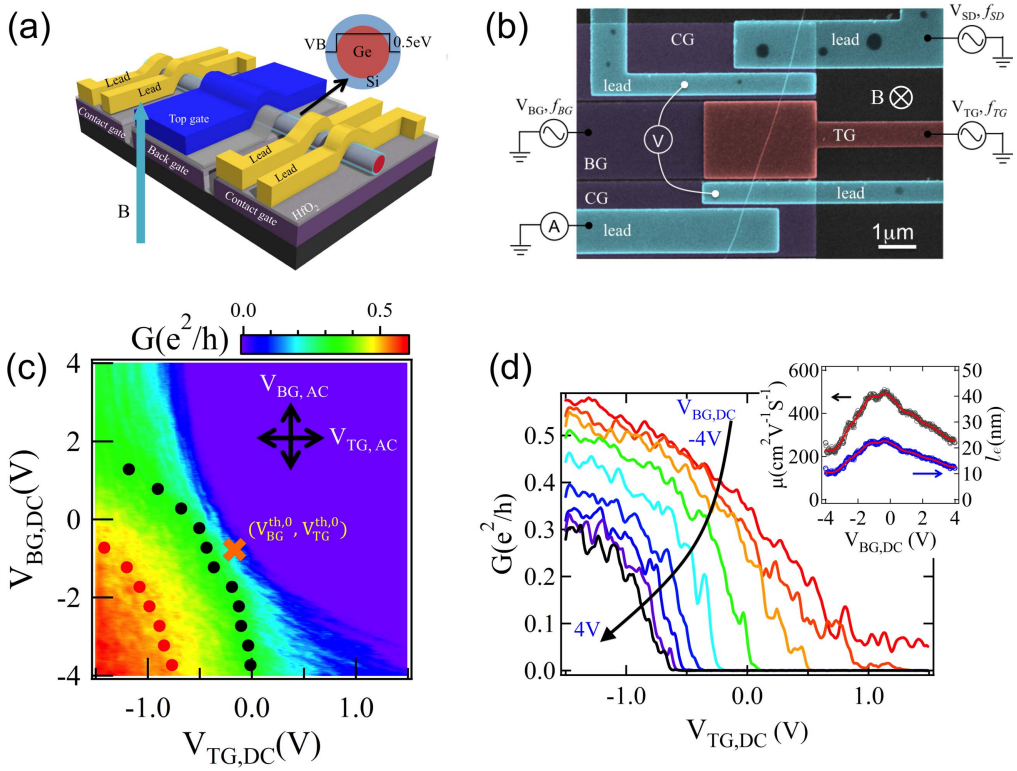

Figure 1. (a) A schematic to illustrate the device architecture. (b) False color SEM image with circuit diagram. (c) Differential conductance G of a 1 μm long Ge/Si device as a function of the TG and BG DC voltage offset. Data was taken at the temperature of 1.5 K. Red and black dots indicate the gate voltages where G is kept constant at $0.5e^2$h and $0.25e^2$h, respectively. The orange cross symbol indicates the intrinsic threshold voltages ($V_{BG}^{th,0}$, $V_{TG}^{th,0}$) where the mobility is highest. Double arrows indicate the small AC signals superimposed on the gates in the magnetic transport. (d) G as a function of $V_{TG,DC}$ corresponding to (c) with $V_{BG,DC}$ varied from −4 to 4 V with 0.5 V steps. UCF is observed on each G trace. The inset shows the gate dependence of the extracted mobility (black circles) and mean free path (blue circles), which are largest when holes accumulate close to the center of the NW. The red solid line is the smooth to guide the eye.

All measurements are conducted at 1.5 K except where noted otherwise. The diameter of the wires is confirmed through atomic force microscopy to be in the range 18–22 nm. Considering the 2–3 nm thick Si shell [13, 14], the diameter of Ge core (W) is around 15 nm. Although the device structure enables a 4-probe electrical measurement (applying and measuring the current from the outer leads while probing the voltage drop across inner leads as shown by the circuit diagram in figure 1(b)), we did not observe any difference between the resistances obtained by 2-probe and 4-probe measurements in all devices. Most likely the doping or scattering effect of the metal contacts interrupts the NW and the inner leads cannot perform as noninvasive probes [35]. Therefore, the data present in the main text are all extracted using the 2-probe electrical measurements.

We first investigated the electrical transport performance with zero B-field using a standard lock-in technique with a 20 μV source-drain AC excitation and a frequency of 137 Hz. The CG voltages were always kept negative to ensure the electrically transparent contacts. Respective DC voltages (denoted as $V_{BG,\ DC}$ and $V_{TG,\ DC}$, respectively) were applied on TG and BG to independently modulate the carrier density (n_{TG} and n_{BG}) and the electrical conductance of the NW. Upon electrical gating, the net carrier density is a result of the sum of both gating effects, $n = n_{TG} + n_{BG}$. The difference between the two contributions breaks the structural inversion symmetry, leading to a build-in electric field across the wire, $E \approx (n_{TG} - n_{BG})/WC_Q$ (for simplicity, we assume that the voltage linearly drops through the wire). Figure 1(c) presents the measured G of a 1 μm long Ge/Si channel as a function of $V_{BG,\ DC}$ and $V_{TG,\ DC}$. The NW tends to pinch off when the gate voltages increase, consistent with the p-type semiconductor nature expected from the ∼0.5 eV VB offset between Ge and Si (see the energy level diagram in the inset of figure 1(a)) [13]. The capacitive ratio of TG and BG (C_{TG} and C_{BG}) is evaluated as $\gamma = C_{TG}/C_{BG} = -\Delta V_{BG}/\Delta V_{TG} \sim 5.5$, where ΔV_{BG} and ΔV_{TG} are gate voltage changes required to maintain a constant conductance (as shown by dots in figure 1(c)). The TG capacitance $C_{TG} \sim 730$ aF ($L = 1$ μm) is estimated from a simple cylinder model with surrounding gates [36]. BG capacitance $C_{BG} = C_{TG}/\gamma \sim$ 130 aF is much smaller than the value extracted from the cylinder-on-plane model [30], implying that the screening of the top metal gate suppresses the BG capacitive coupling. The conductance traces as a function of V_{TG} are plotted in figure 1(d). The device can be completely pinched off with sufficiently positive gate voltage. By increasing V_{BG} the conductance trace trend is shifted to more negative V_{TG}, indicating the variation of threshold voltage of the measured device. The hole mobilities of the

device were calculated from the slope of the sub-threshold region with Drude's model [14, 30]:

$$\mu = \frac{G}{ne} = \frac{\mathrm{d}G}{\mathrm{d}V_{\mathrm{TG}}} \times \frac{L^2}{C_{\mathrm{TG}}}, \quad (1)$$

where μ is the mobility and e is the single hole charge. The mobility exhibits a non-monotonic relation to the back gate voltage (and a similar dependence on the TG voltage). The mobility first increases from $200\,\mathrm{cm^2\,V^{-1}\,s^{-1}}$ to $500\,\mathrm{cm^2\,V^{-1}\,s^{-1}}$ with $V_{\mathrm{BG,DC}}$ tuned from -4 to -0.5 V, and then drops back to around $200\,\mathrm{cm^2\,V^{-1}\,s^{-1}}$ as $V_{\mathrm{BG,DC}}$ is further increased to 4 V. This result indicates that the carriers are scattered in the transport by the interfacial impurities or defects when pushed/pulled closer to the upper/lower Ge/Si interfaces. The mean free path $l_{\mathrm{e}} = \nu_{\mathrm{F}}\tau_{\mathrm{e}} = m^*\nu_{\mathrm{F}}\mu/\mathrm{e}$ is evaluated in the range 10–20 nm, where $m^* = 0.28m_{\mathrm{e}}$ is the effective mass of heavy holes in Ge/Si NW, m_{e} is the free electron mass, ν_{F} is the Fermi velocity and τ_{e} is the elastic scattering time. Evaluated l_{e} and μ as a function of $V_{\mathrm{BG,DC}}$ is plotted in the inset of figure 1(d). The mean free path $l_{\mathrm{e}} \sim W \ll L$ indicates a quasi one-dimensional diffusive transport regime in the NW. The cross symbol in figure 1(c) indicates the intrinsic threshold voltages $(V_{\mathrm{BG}}^{\mathrm{th},0},\ V_{\mathrm{TG}}^{\mathrm{th},0}) = (-0.5\ \mathrm{V},\ -0.08\ \mathrm{V})$ obtained from the conductance trace with the highest mobility where the interfacial dipole gating is minimized by the external electrical field and the holes were dominantly located in the center of the wire. The gate dependence of the net carrier density can be expressed as:

$$n = n_{\mathrm{TG}} + n_{\mathrm{BG}} = C_{\mathrm{TG}}(V_{\mathrm{TG,DC}} - V_{\mathrm{TG}}^{\mathrm{th},0}) + C_{\mathrm{BG}}(V_{\mathrm{BG,DC}} - V_{\mathrm{BG}}^{\mathrm{th},0}). \quad (2)$$

Equation (2) will reduce to $n = 2C_{\mathrm{TG}}(V_{\mathrm{TG,DC}} - V_{\mathrm{TG}}^{\mathrm{th},0})$ or $2C_{\mathrm{BG}}(V_{\mathrm{BG,DC}} - V_{\mathrm{BG}}^{\mathrm{th},0})$ when the built-in electric field is zero (where $n_{\mathrm{TG}} = n_{\mathrm{BG}}$). It is worthwhile pointing out that on each conductance trace we observe notable fluctuations, which may originate from the so-called universal conductance fluctuation (UCF). The phenomenon is indicative of the quantum interference of electron wavefunction induced by scattering events and is always amplified in coherent transport device [37].

The presence of the UCF may mask the features of MC induced by the quantum correlations of the weak-(anti)localization complicating the analysis [23, 24, 27, 28]. To recover a WL (or WAL) signal from the UCF perturbation we averaged the MC at each DC voltage offset and magnetic field by consistently superimposing small AC signals on both TG and BG. The modulations on both gates are produced using a digital-analog convertor (DAC). As shown in figure 2(a), the red and blue curves are the respective triangle voltage waveforms of TG and BG ($V_{\mathrm{TG,\ AC}}$ with $f_{\mathrm{TG}} = 10$ Hz and $V_{\mathrm{BG,\ AC}}$ with $f_{\mathrm{BG}} = 1$ Hz) in a 2 s time span. The black plot shows the corresponding real time source-drain differential conductance recorded from the lock-in amplifier using a digitizer. The periodic fluctuations of G reflect the variations of the gate voltages. The averaged conductance over the time span, which is an integer multiple of the period of the TG and BG modulations, is recorded for each data point. The average is equivalent to the mean conductance value over a small TG and BG voltage window as indicated by the double arrows in figure 1(c). Figure 2(b) presents the comparison of the MC of a 1 μm long device with different AC gate voltage amplitude in a B-field range of ± 9 T at $G(0) \sim 0.3\ \mathrm{e^2\,h^{-1}}$, where $G(0)$ is the conductance at zero B. With sufficient AC amplitude (usually $<10\%$ of the whole DC scan range) the UCF is largely suppressed, which enables a good fitting with the theory models in the data analysis. The magnetoresistance (MR) plots of three devices with $L = 1\ \mu$m, 2 μm and 5 μm are compared in figure 2(c). The amplitude of MR relates linearly to the channel length while the lineshapes are similar for all threes device with a sharp valley at low B and a steadily increasing resistance at large B. The negative MR at low B implies the presence of WAL and spin relaxation in the Ge/Si NWs. The slow increase of MR at large magnetic field may be a result of classical magnetoresistance (CMR) due to the hole trajectory bending, proportional to $(\mu B)^2$ [38]. Giant linear magnetic resistance is observed in the topological insulators and narrow gap semiconductors due to fluctuations of mobility, but the case does not apply for our devices [38–41]. The relative changes of MC, $\Delta G/G(0) = (G(B) - G(0))/G(0)$, are presented in figure 2(d), where $G(B)$ is the conductance at a given B-field. Each trace of the three devices appears as a positive peak with different amplitudes and widths. The contrast of the MC in different devices implies discrepancies of the microscopic scattering pattern and the physical characteristic lengths.

Discussion

To interpret the microscopic magnetic transport mechanism, we investigated the evolution of MC on the dependence of the carrier density and the electric field. Measurements on the three devices with different lengths are similar; hence we focus on the results of the 1 μm long Ge/Si device. Figure 3(a) shows the MC traces (black circles) in the B-field range ± 9 T with variation of $V_{\mathrm{TG,DC}}$ from -1.5 V to 0.5 V while $V_{\mathrm{BG,DC}}$ is maintained at -4 V. The measured conductance is in the range $G_0 = 0.15 \sim 0.6\ \mathrm{e^2\,h^{-1}}$, corresponding to a carrier density $n = 0.7 \sim 7 \times 10^9\ \mathrm{m^{-1}}$. The Fermi wavelength $\lambda_{\mathrm{F}} = (2\pi^2W^2/3n)^{1/3} \sim 9 \sim 12$ nm, indicating $M = 4W/\lambda_{\mathrm{F}} \sim 6 \sim 8$ subband modes [29]. Each MC trace displays a peak at zero B-field which is in some cases accompanied by two weak side shoulders at moderate B. This result indicates the existence of the WAL effect on the hole transport over a wide range of carrier density. WAL quantum correction to the classical diffusive conductance was quantitatively analyzed by a one-dimensional model in a 'pure' regime taking into account the flux cancellation induced by

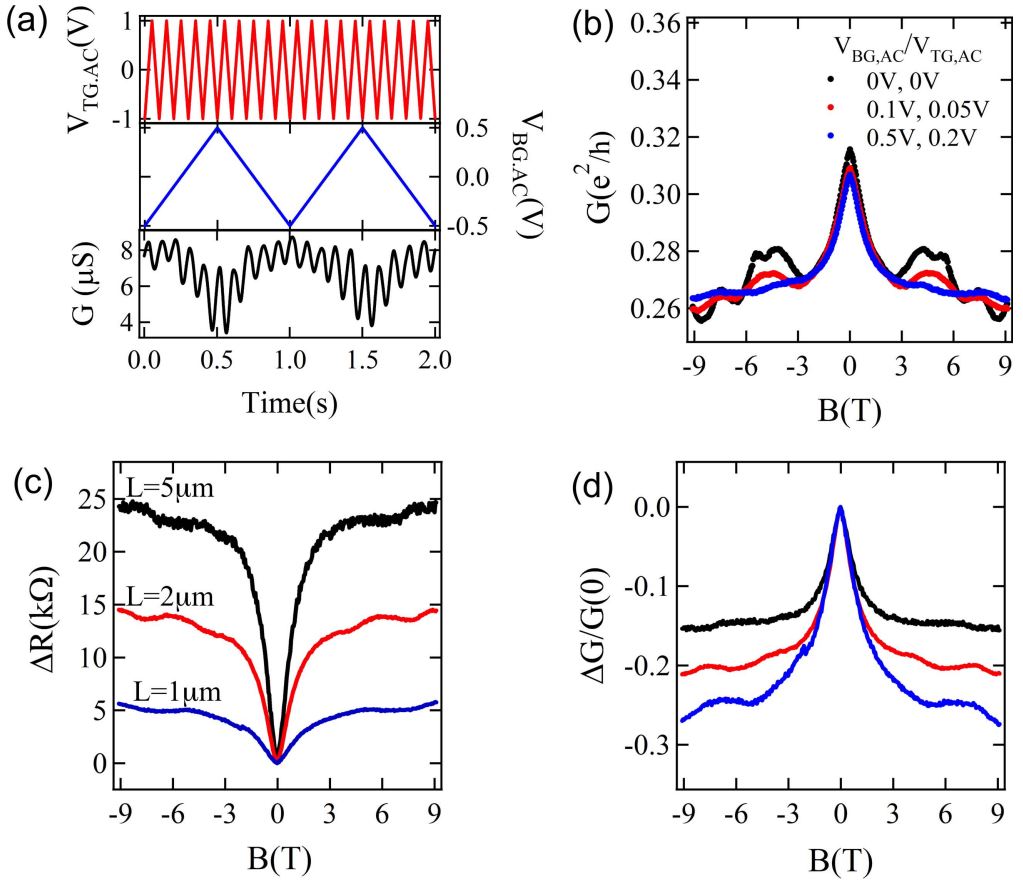

Figure 2. (a) Real time signals of TG (red), BG (blue) AC voltages and measured differential conductance G (black) in a 2 s span. The recorded G is the average of all signal collected in 2 s. (b) Comparison of G as a function of magnetic field with different $V_{\mathrm{TG,AC}}$ and $V_{\mathrm{BG,AC}}$. UCF is dramatically suppressed by averaging the MC with sufficient AC gate voltages. (C) MR and (d) relative MC of three devices with channel lengths of 1 μm (blue), 2 μm (red) and 5 μm (black), respectively.

the boundary scattering [24, 28–30, 42]:

$$G(B) = G_{\infty} - \frac{2e^2}{hL} \times \left[\frac{3}{2}\left(\frac{1}{l_{ph}^2} + \frac{4}{3l_s^2} + \frac{1}{l_B^2}\right)^{-\frac{1}{2}} - \frac{3}{2}\left(\frac{1}{l_{ph}^2} + \frac{4}{3l_s^2} + \frac{1}{l_e^2} + \frac{1}{l_B^2}\right)^{-\frac{1}{2}} - \frac{1}{2}\left(\frac{1}{l_{ph}^2} + \frac{1}{l_B^2}\right)^{-\frac{1}{2}} + \frac{1}{2}\left(\frac{1}{l_{ph}^2} + \frac{1}{l_e^2} + \frac{1}{l_B^2}\right)^{-\frac{1}{2}} \right]. \quad (3)$$

Here, G_{∞} is the classical conductance without quantum correction. l_{ph} is the phase decoherence length, and l_{s} is the spin scattering length. The magnetic dephasing length $l_B^2 = C_1 l_{\mathrm{e}} l_m^4/W^3 + C_2 l_{\mathrm{e}}^2 l_m^2/W^2$ is obtained according to the Beenakker and van Houten model [42], where $l_m = (\hbar/eB)^{1/2}$ and constants $C_1 = 9.5(4\pi)$ and $C_2 = 4.8$ (3) are geometrical coefficients for the case of specular (diffusive) boundary scattering [42]. The characteristic lengths are also related to the corresponding times: $l_{\mathrm{ph,s},B}^2 = D\tau_{\mathrm{ph,s},B}$, where $D = l_{\mathrm{e}} v_{\mathrm{F}}/2$ is the diffusive coefficient. τ_{ph}, τ_{s} and τ_B are the phase decoherence, spin life and magnetic dephasing time, respectively. We note that we were unable to obtain physical values by fitting with a 'dirty' regime model [24, 26].

To obtain least square fitting on the measured MC over the whole magnetic field range, a parabolic background from CMR controlled by the mobility ($\sim(\mu B)^2$) is added to equation (3). Figure 3(b) shows a comparison of the simulation results of WAL correction to conductance with (open dots) and without (solid lines) the CMR correction. Values of l_{ph} and l_{s} used for the simulation are close to the typical values evaluated from similar NW devices [28–30] and the mobility is 200 cm^2 V^{-1} s^{-1}. Without CMR the MC exhibits an upturn at moderate B, which is often seen where the WAL is lifted due to the magnetic flux as $\tau_B \leqslant \tau_{\mathrm{s}}$ (indicating crossover to the WL regime). Upon adding CMR the features of the crossover between WAL and WL are weakened [38, 43]. The simulation captures the main features of the measured data in figure 3(a). Each MC trace can be fitted well with the 'WAL + CMR' model as shown by the red solid lines. Fixed parameters l_{e} and μ, which vary with the gate voltages, are extracted from the field-effect transport curves and are evaluated with values shown in the inset of figure 1(d). G_{∞}, l_{ph} and l_{s} are free fitting parameters. The fitting residuals (differences between fits and data) of each curve fall in a range ± 0.003 e^2 h^{-1}, which is smaller than 5% of the measured quantum correction to the conductance. In figure 3(c) we plot

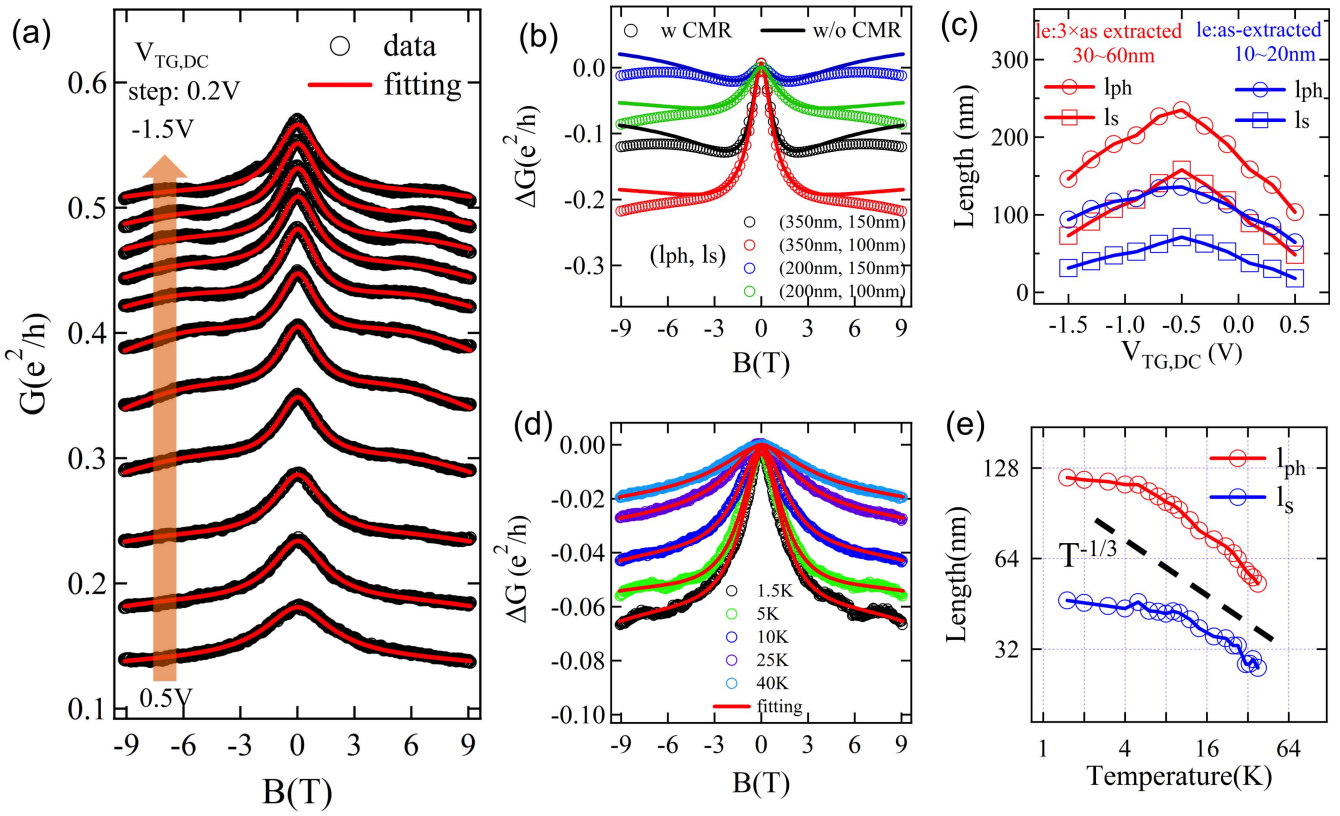

Figure 3. (a) MC traces for a 1 μm channel with $V_{\mathrm{TG,DC}}$ varied from 0.5 to -1.5 V with 0.2 V steps and $V_{\mathrm{BG,DC}}$ fixed at -4 V. Black circles represent the experimental data, red solid lines are the fits using the input parameters l_e and μ extracted at each set of gate voltage conditions from the field-effect transport curves in figure 1. (b) Simulation comparison of the WAL correction to the conductance with (circles) and without (solid line) the classical magnetoresistance background. (c) Extracted phase decoherence length l_{ph} (circles) and spin scattering length l_s (open squares) with different fitting parameters l_e. Blue symbols are the fitting results using the evaluated l_e and μ. Red symbols show fitting results using three times larger l_e and μ for comparison. (d) Evolution of MC at different temperature (T) from 1.5 K to 40 K at $V_{\mathrm{BG,DC}} = -4$ V and $V_{\mathrm{TG,DC}} = -1$ V. The red solid lines indicate the fitting. (e) l_{ph} (red) and l_s (blue) as a function of T in a log–log plot. The black dash-line indicates a $T^{-1/3}$ power law.

l_{ph} and l_s as a function of $V_{\mathrm{TG,DC}}$ (blue symbols). Both l_{ph} and l_s first increase and subsequently decrease with increasing $V_{\mathrm{TG,DC}}$. This observation is in contrast to previous reports on InAs and InSb NWs [25–28], where the l_{ph} always decreases with reducing carrier density because of the enhanced electron–electron inelastic scattering rate [28, 44]. The non-monotonic behavior of l_{ph} and l_s in the present device implies a complicated microscopic scattering mechanism, which perhaps varies with a combined effect of the carrier density, mean free path and the electric field. To clarify the flux cancellation effect by the boundary scattering (where $l_e \geqslant W$) as described by the model of Beenakker and van Houten [42], we obtained a comparative set of l_{ph} and l_s (red symbols) on the same experimental data by assuming the input parameter l_e three times larger than the extracted mean free path. The apparent (or fitted out) l_{ph} and l_s increase with the input parameter l_e roughly following a function of $\sim\sqrt{l_e}$, consistent with the definition of l_B^2 in equation (3). The results indicate that the thin diameters of NWs or large mean free path will hinder the magnetic field induced dephasing of carriers. As a crosscheck, we also extracted $l_{\mathrm{ph}} \sim 100$ nm from the auto-correlation analysis of the UCF in the MC curves without AC gate modulation, in good agreement with the WAL fittings.

Figure 3(d) shows MC traces for different temperature (T) and $n = 6 \times 10^9\ \mathrm{m}^{-1}$. Here fitting is performed using l_e and μ evaluated at $T = 1.5$ K. The amplitudes of the MC become smaller with a broadened peak as T is increased. The characteristic lengths as a function of T are plotted in figure 4(e). The evaluated l_{ph} decays as $\sim T^{-1/3}$ when T is above 5 K, indicating that the charge decoherence is dominated by the Nyquist process in the one-dimensional system, where hole–hole inelastic scattering occurs with small energy exchange [30, 41, 45].

Spin relaxation in diffusive systems can occur via Elliott-Yafet (EY) effect [46] or D'yakonov–Perel (DP) mechanism [47]. The EY model attributes the spin randomization due to scattering at spin–orbit coupled (SOC) impurities and the spin relaxation length $l_{s,EY} = \sqrt{\frac{3}{8}}\frac{E_G}{E_F} l_e \frac{(E_G+\Delta_{SO})(3E_G+2\Delta_{SO})}{\Delta_{SO}(2E_G+\Delta_{SO})}$ $\sim 500 - 1000$ nm, with Ge direct band gap $E_G = 0.9$ eV, spin–orbit gap $\Delta_{SO} = 0.29$ eV [17], Fermi energy $E_F < 80$ meV and l_e in the range 10–20 nm depending on the applied gate voltages. Spin relaxation length estimated with the EY model ($l_{s,\,EY}$) is negligible compared with the evaluated l_s in our WAL measurement. The spin distorted between the random scattering events as described by the DP mechanism was considered to dominate the spin lifetime τ_s

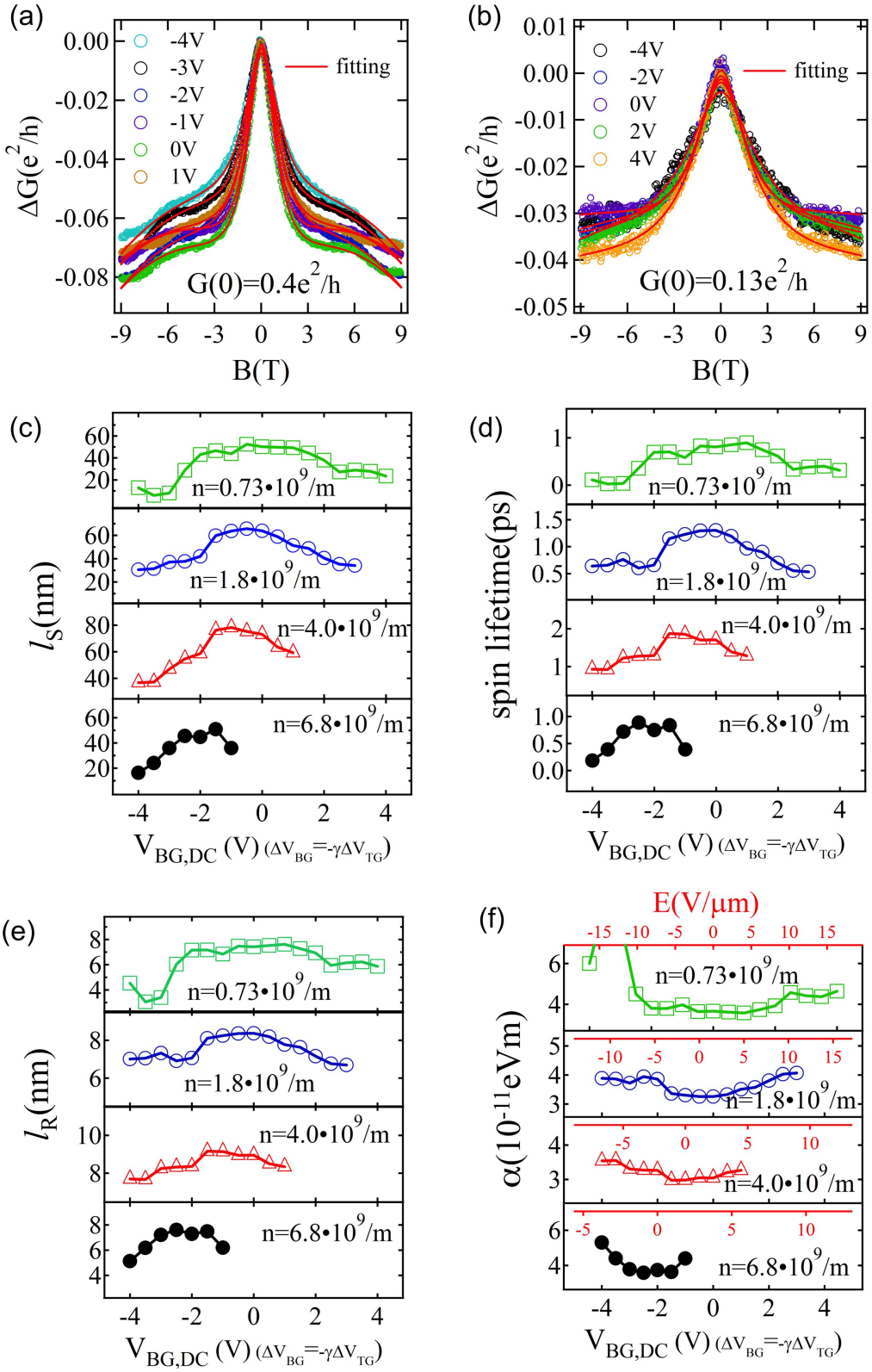

Figure 4. Evolution of the MC curves when TG and BG are simultaneously tuned to maintain a constant $G(0)$ of (a) 0.4 $e^2\,h^{-1}$, and (b) 0.13 $e^2\,h^{-1}$. The relationship linking values of TG and BG voltage is $\Delta V_{BG} = -\gamma \Delta V_{TG}$. Red solid lines are the fits using the input parameters l_e and μ of each gate voltages according to the inset of figure 1(d). Extracted (c) spin scattering length l_s, (d) spin lifetime, (e) spin precession length l_R, and (f) Rashba coefficient α as a function of the asymmetric gating. In figure 4(f) the tuned electrical field across the nanowire is plotted on the inset top axis.

(or l_s) [47]. Both bulk Si and Ge are inversion symmetric [17, 48], such that the Dresselhaus effect is absent in the Ge/Si core/shell NWs. Rashba spin–orbit interaction (RSOI) from the structural inversion asymmetry will lead to the spin splitting of the band and determine the resonant spin precession length l_R. The DP mechanism holds well for two and three-dimensional diffusive transport systems without geometrical confinement where $\tau_S \propto \tau_e^{-1}$. As discussed above the diffusion coefficient $D = l_e \upsilon_F/2 \propto \tau_e$ indicating that l_s is independent of l_e (or τ_e) in the systems without geometrical confinement. However, the measured l_s in Ge/Si NWs exhibits a clear dependence on the gate voltages and therefore l_e (figure 3(c)). To interpret the deviation between the experiments and the theory, the suppression of spin relaxation due to the dimensional confinement must be taken into account. The enhancement of the spin lifetime has been observed in the InAs NWs and narrow strips of etched InGaAs quantum wells [25, 49]. The model developed by Kettemann describes the relationship of τ_s (or l_s) with l_R, l_e and W, considering the cancellation of both spin precession and magnetic flux due to boundary scattering [50]:

$$\frac{1}{l_s^2} = \frac{1}{D\tau_s} = \frac{W^3}{C_3 l_e l_R^4}, \tag{4}$$

with geometrical constant $C_3 = 130$. l_R denotes the spin precession length over which the spins will flip in a material with a spin–orbit coupled band structure. l_s marks the characteristic length over which the spins experience relaxations. As discussed above, in the Ge/Si NWs we attribute the spin relaxation to the DP mechanism with the existence of Rashba type SOC. The spin relaxation length l_s can be determined by l_R once the scattering patterns and the dimensions are given. Using equation (4) and l_s in figure 3(c) we calculate $l_R = 4$–10 nm, corresponding to a Rashba SOI coefficient $\alpha = \hbar^2/m^* l_R = 3 \sim 6 \times 10^{-11}$ eVm, and spin splitting energy $E_{\mathrm{RSOI}} = \hbar^2/2m^* l_R^2 = 1.5 \sim 3$ meV with $\hbar = h/2\pi$ where h is the Plank constant [17, 28]. The SOI energy is almost one order larger than previously reported values in InAs, InSb and GeSi core/shell NWs [25–30].

We further investigated the electric field control of the SOI strength in our Ge/Si NW devices. TG and BG voltages were tuned simultaneously with the relation $\Delta V_{\mathrm{BG}} \approx -\gamma \Delta V_{\mathrm{TG}}$ (as indicated by the dots in figure 1(c)) in order to keep the conductance constant but vary the electric field across the wire that induces the DRSOI. As discussed above the built-in electrostatic field is proportional to the carrier distribution asymmetry, $E \propto (n_{\mathrm{TG}} - n_{\mathrm{BG}})$. At each n, values of $V_{\mathrm{TG,\,DC}}$ and $V_{\mathrm{BG,DC}}$ required to balance the carrier distribution (to minimize E) are determined by equation (2). Figures 4(a) and (b) show MC traces and fittings when asymmetric voltage gating is applied with $G(0)$ fixed at $0.4\ e^2\ h^{-1}$ and $0.13\ e^2\ h^{-1}$. Only the value of $V_{\mathrm{BG,\,DC}}$ is indicated in the legend but note that $V_{\mathrm{TG,\,DC}}$ is also varied. The lineshapes of the MC traces show variations as the gate voltages are altered. Figure 4(c) shows the fitted results for spin relaxation length l_s as a function of $V_{\mathrm{BG,DC}}$ at different carrier densities. A broad peak-like feature in l_s is always observed with 2–3 times change and the $V_{\mathrm{BG,\,DC}}$ position of the maximum l_s shifts with n. The spin lifetime $\tau_s = l_S^2/D$ exhibits a 2–10 fold variation (figure 4(d)), which is a combined result of the variations of l_e and l_R according to the Kettemann model [50]. By improving the lithography processes to fabricate cleaner devices, we expect the spin lifetime τ_s will be prolonged by one or two more orders (l_e up to 500 nm have been reported [13]). Equations (3) and (4) are only valid for the WAL analysis in the diffusive transport system with sufficient scattering events. In the ballistic transport regime of quantum dots or short channels with the absence of scattering, the coherent spin precession always persists and the spin relaxation from the D'yakonov–Perel mechanism is completely suppressed, implying an infinite τ_S according to the WAL theory. In reality under such circumstances the spin decoherence caused by the charge noise surrounding the device through the SOI or the paramagnetic impurities in the leads should be taken into account. With equation (4) the Rashba spin precession length l_R that removes the cancellation effects of the flux and spin precession is evaluated and plotted as a function of gate voltages and carrier densities in figure 4(e). A 20%–50% change of l_R is achieved through modulation by the gating. The maximum value always appears around the positions where the system is most balanced $n_{\mathrm{TG}} = n_{\mathrm{BG}}$. Correspondingly, the Rashba SOI coefficient α is smallest when E inside the NWs is minimized as shown in figure 4(f). For simplicity, we assume a parallel-plate model and that the band bending induced built-in electrical field linearly drops across the NW. The asymmetric gating induced electrical field is estimated as $E = (n_{\mathrm{BG}} - n_{\mathrm{TG}})/WC_Q$ with $C_Q = e\partial n(E_F)/\partial E_F$ and the one-dimensional carrier density $n(E_F) = (W^2/12\pi)(2m^* E_F/\hbar^2)^{3/2}$. In figure 4(f) the Rashba SOI coefficient α as a function of E is also plotted using the inset X-axis. $E = 0$ here indicates that the built-in field is minimal considering the asymmetric gating. The calculation yields a field variation inside the NW of up to $\sim 4\mathrm{V}\mu\mathrm{m}^{-1}$ with the carrier density of $n \sim 7 \times 10^9\ \mathrm{m}^{-1}$, according to the change of $\alpha \sim 2 \times 10^{-11}$ eVm. The Rashba constant is evaluated as $\alpha_0 = \alpha/eE \approx 5\ \mathrm{nm}^2$, which is one order larger than the conventional bulk Rashba constant $\sim 0.4\ \mathrm{nm}^2$, implying the existence of the large dipole coupled SOI in the Ge/Si NWs as the DRSOI theory predicts [17]. With lower carrier density the E variation becomes larger as the screening ability of the NW drops. For lower density we did not observed a larger change of α, implying that α_0 becomes smaller when the NW is pinched off.

We did not observe l_R decreasing to zero when the dual gate controlled carrier distribution is most balanced, implying that electrical gating symmetry can be improved or that other sources of spin relaxation exist in the Ge/Si NWs. Similar results were reported on the electric field tuned InAs NWs by Scherübl *et al* [27] where they attributed the lack of quenching of l_R to the presence of the finite Dresselhaus SOI, asymmetry confinement potential, or scatterings by spin–orbit coupled impurities. In the case of the Ge/Si NW the Dresselhaus effect is neglected but the geometrical asymmetry between TG and BG needs to be taken into account, as the built-in electric field induced by the dual gating may never be

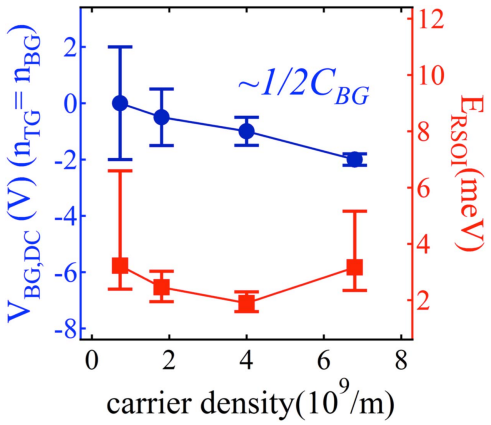

Figure 5. The BG voltage (blue dots) corresponding to the balanced gating condition ($n_{TG} = n_{BG}$) varies with carrier density in a linear relation $\sim 1/2C_{BG}$ as equation (2). The blue error bars indicate the voltage range where the characteristic lengths change by less than 10% in figure 4. SOI energy (red squares) shows a weak dependence on the carrier density. The red error bars calculated from the Rashba coefficient of figure 4 indicates the energy distribution modulated by the asymmetric gating.

completely cancelled. For clarity values of $V_{BG,\,DC}$ at which we evaluate the largest l_s (where $n_{TG} = n_{BG}$) are plotted as a function of n in the figure 5. Values display a linear dependence on n with a slope of $\sim 1/2C_{BG}$ consistent with the prediction of equation (2). The averaged direct Rashba spin–orbit energy of $E_{RSOI} = 2$–4 meV is calculated as indicated by the red squares in figure 5, and exhibits no clear dependence on n. The red error bars indicate the distribution of E_{RSOI} controlled by dual gating with different carrier densities. The maximal change of E_{RSOI} can be up to ~ 3 times.

Conclusion

The carrier density and electrical field inside the Ge/Si core/shell nanowires are controlled by an independent top and back gating configuration. Under an external magnetic field the SOI of the nanowires is analyzed from the weak-antilocalization feature in the MC. With constant carrier density the electrical field across the nanowire from the asymmetric gating modulates both the mean free path and the strength of SOI. Larger mean free path is observed when holes are confined close to the wire center, leading to longer spin lifetime due to the cancellation of spin precession in a confined geometry. With a variable carrier density in the nanowire the spin–orbit energy is evaluated in the range 1–6 meV, which is almost one order larger than that reported for InSb or InAs nanowires. The spin–orbit energy is tuned by a factor of up to ~ 3 with electrostatic field, and the corresponding Rashba coefficient is $\sim 5\,\mathrm{nm}^2$. The strong and tunable SOI provides evidence for the theoretically predicted DRSOI in the Ge/Si core/shell nanowire system. These results indicate that the Ge/Si core/shell nanowires are a promising system for spin-related quantum information processing.

Methods

Transfer of Ge/Si NWs

The NWs are precisely positioned onto predefined bottom gates using a Polyvinyl alcohol/Poly(methylmethacrylate) (PVA/PMMA) polymer bilayer technique, which is commonly used for the transfer of the layered 2D materials [33] and other NWs [34]. Briefly, a 6% PVA aqueous solution is firstly spun onto a Si wafer at 1000 rmp for 60 s and baked on a hotplate at 75 °C for three minutes. The PMMA (Microchem, 950 K A6) is cast on the PVA surface at 1000 rmp for 60 s and baked at 75 °C for ten minutes. A batch of Ge/Si NWs are picked up from the growth substrate and transferred to the PMMA surface with a tungsten probe coated with a lump of Polydimethylsiloxane. The PMMA film is then attached on a glass frame carrier using adhesive tape (Nitto BTK-180E-BLK) and peeled off from the PVA surface with the silicon wafer placed on a hotplate at 75 °C. The carrier frame with the polymer film is then mounted on a home-made micromanipulator with a precision of 1 μm. A target Ge/Si NW is relocated under an optical microscope with a dark field objective. The PMMA film with NW are brought into contact with the sample surface. After the PMMA has adhered to the surface the substrate is heated up to 150 °C and the frame carrier is gradually lifted to break the PMMA film. The PMMA with NWs are finally left on the target chip and the PMMA is removed using acetone.

Fabrication and measurement of Ge/Si NW FETs

The devices are fabricated with standard electron beam lithography and electron beam deposition. Three 5/25 nm Ti/Au bottom gates, separated into two contact and one channel gate, are firstly deposited on a highly-doped Si chip capped with a 300 nm SiO_2 insulating layer. A 5 nm thick HfO_2 high-κ dielectric layer grown at 80 °C by ALD covers all the bottom gates. After NWs are transferred onto the bottom gates 4-terminal 1/70 nm thick Ti/Pd leads are patterned and deposition after a 3 s BHF etching. An additional 5 nm HfO_2 ALD top layer was then grown at 80 °C followed with the deposition of a 5/50 nm Ti/Au TG on the transport channel segment. The conductance of the devices is measured using a lock-in technique with an AC voltage excitation of 20 μV and a frequency of 137 Hz. In the electrical transport only DC voltages are applied on the top and bottom gates. In the magnetic transport small AC signals ($V_{TG,AC}$ with $f_{TG} = 10$ Hz and $V_{BG,\,AC}$ with $f_{BG} = 1$ Hz) are superimposed on each gate to average out the UCF. The persistent gate modulations (triangle waveforms) adding on both gates are produced using a DAC. The real time differential conductance from the lock-in is then collected by a digitizer over a time span which is an integer multiple of the periods of both TG and BG modulations. The conductance sequence is averaged and recorded as a data point at each gate voltage offset and magnetic field.

Acknowledgments

We thank M Kohda, J Nitta, P Stano and D Loss for useful discussion. R S Deacon acknowledges support from Grants-in-Aid for Young Scientists B (No. 26790008). The work was partially supported by Grants-in-Aid for Scientific Research (A) (No. 15H02015) and Grants-in-Aid for Scientific Research on Innovative Areas 'Science of hybrid quantum systems' (No. 15H05867).

References

[1] Datta S and Das B 1990 Electronic analog of the electro-optic modulator *Appl. Phys. Lett.* **56** 665–7
[2] Manchon A, Koo H C, Nitta J, Frolov S M and Duine R A 2015 New perspectives for Rashba spin–orbit coupling *Nat. Mater.* **14** 871–82
[3] Lutchyn R M, Sau J D and Das Sarma S 2010 Majorana Fermions and a topological phase transition in semiconductor-superconductor heterostructures *Phys. Rev. Lett.* **105** 077001
[4] Gangadharaiah S, Braunecker B, Simon P and Loss D 2011 Majorana edge states in interacting one-dimensional systems *Phys. Rev. Lett.* **107** 036801
[5] Mourik V, Zuo K, Frolov S M, Plissard S R, Bakkers E P A M and Kouwenhoven L P 2012 Signatures of Majorana Fermions in hybrid superconductor-semiconductor nanowire devices *Science* **336** 1003–7
[6] Deng M T, Vaitiekėnas S, Hansen E B, Danon J, Leijnse M, Flensberg K, Nygård J, Krogstrup P and Marcus C M 2016 Majorana bound state in a coupled quantum-dot hybrid-nanowire system *Science* **354** 1557–62
[7] Nowack K C, Koppens F H L, Nazarov Y V and Vandersypen L M K 2007 Coherent control of a single electron spin with electric fields *Science* **318** 1430–3
[8] Nadj-Perge S, Frolov S M, Bakkers E P A M and Kouwenhoven L P 2010 Spin–orbit qubit in a semiconductor nanowire *Nature* **468** 1084–7
[9] van den Berg J W G, Nadj-Perge S, Pribiag V S, Plissard S R, Bakkers E P A M, Frolov S M and Kouwenhoven L P 2013 Fast spin–orbit qubit in an Indium Antimonide nanowire *Phys. Rev. Lett.* **110** 066806
[10] Petersson K D, McFaul L W, Schroer M D, Jung M, Taylor J M, Houck A A and Petta J R 2012 Circuit quantum electrodynamics with a spin qubit *Nature* **490** 380–3
[11] Dresselhaus G 1955 Spin–orbit coupling effects in Zinc Blende structure *Phys. Rev.* **100** 580–6
[12] Rashba E I 1960 Properties of semiconductors with an extremum loop. 1. Cyclotron and combinational resonance in a magnetic field perpendicular to the plane of the loop *Sov. Phys. Solid State* **2** 1224–38
[13] Lu W, Xiang J, Timko B P, Wu Y and Lieber C M 2005 One-dimensional hole gas in germanium/silicon nanowire heterostructures *Proc. Natl Acad. Sci. USA* **102** 10046–51
[14] Xiang J, Lu W, Hu Y, Wu Y, Yan H and Lieber C M 2006 Ge/Si nanowire heterostructrues as high-performance field-effect transistors *Nature* **441** 489–93
[15] Roddaro S, Fuhrer A, Brusheim P, Fasth C, Xu H Q and Samuelson L 2008 Spin states of holes in Ge/Si nanowire quantum dots *Phys. Rev. Lett.* **101** 186802
[16] Hu Y, Kuemmeth F, Lieber C M and Marcus C M 2012 Hole spin relaxation in Ge-Si core–shell nanowire qubits *Nat. Nanotechnol.* **7** 47–50
[17] Kloeffel C, Trif M and Loss D 2011 Strong spin–orbit interaction and helical hole states in Ge/Si nanowires *Phys. Rev.* B **84** 195314
[18] Nitta J, Akazaki T and Takayanagi H 1997 Gate control of spin–orbit interaction in an inverted $In_{0.53}Ga_{0.47}As/In_{0.52}Al_{0.48}As$ heterostructure *Phys. Rev. Lett.* **78** 1335
[19] Heida J P, van Wees B, Kuipers J J, Klapwijk T M and Borghs G 1998 Spin–orbit interaction in a two-dimensional electron gas in a InAs/AlSb quantum well with gate-controlled electron density *Phys. Rev.* B **57** 11911
[20] Fasth C, Fuhrer A, Samuelson L, Golovach V N and Loss D 2007 Direct measurement of the spin–orbit interaction in a two-electron InAs nanowire quantum dot *Phys. Rev. Lett.* **98** 266801
[21] Takahashi S, Deacon R S, Yoshida K, Oiwa A, Shibata K, Hirakawa K, Tokura Y and Tarucha S 2010 Large anisotropy of the spin–orbit interaction in a single InAs self-assembled quantum dot *Phys. Rev. Lett.* **104** 246801
[22] Kanai Y, Deacon R S, Takahashi S, Oiwa A, Yoshida K, Shibata K, Hirakawa K, Tokura Y and Tarucha S 2011 Electrically tuned spin–orbit interaction in an InAs self-assembed quantum dot *Nat. Nanotech.* **6** 511–6
[23] Bergmann G 1984 Weak localization in thin films: a time-of-flight experiment with conduction electrons *Phys. Rep.* **107** 1–58
[24] Hansen A E, Björk M T, Fasth C, Thelander C and Samuelson L 2005 Spin relaxation in InAs nanowires studied by tunable weak antilocalizaiton *Phys. Rev.* B **71** 205328
[25] Roulleau P, Choi T, Riedi S, Heinzel T, Shorubalko I, Ihn T and Ensslin K 2010 Suppression of weak antilocalization in InAs nanowires *Phys. Rev.* B **81** 155449
[26] Liang D and Gao X P A 2012 Strong tuning of Rashba spin–orbit interaction in single InAs nanowires *Nano Lett.* **12** 3263–7
[27] Scherübl Z, Fülöp G, Madsen M H, Nygård J and Csonka S 2016 Electrical tuning of Rashba spin–orbit interaction in multigated InAs nanowires *Phys. Rev.* B **94** 035444
[28] van Weperen I, Tarasinski B, Eeltink D, Pribiag V S, Plissard S R, Bakkers E P A M, Kouwenhoven L P and Wimmer M 2015 Spin–orbit interaction in InSb nanowires *Phys. Rev.* B **91** 201413
[29] Higginbotham A P, Kuemmeth F, Larsen T W, Fitzpatrick M, Yao J, Yan H, Lieber C M and Marcus C M 2014 Antilocalization of Coulomb blockade in a Ge/Si nanowire *Phys. Rev. Lett.* **112** 216806
[30] Hao X J, Tu T, Cao G, Zhou C, Li H O, Guo G C, Fung W Y, Ji Z, Guo G P and Lu W 2010 Strong and tunable spin–orbit coupling of one-dimensional holes in Ge/Si core/shell nanowires *Nano Lett.* **10** 2956–60
[31] Lauhon L J, Gudiksen M S, Wang D L and Lieber C M 2002 Epitaxial core–shell and core-multishell nanowire heterostructures *Nature* **420** 57–61
[32] Yao J, Yan H, Das S, Klemic J F, Ellenbogen J C and Lieber C M 2014 Nanowire nanocomputer as a finite-state machine *Proc. Natl Acad. Sci. USA* **111** 2431–5
[33] Taychatanapat T, Watanabe K, Taniguchi T and Jarillo-Herrero P 2013 Electrically tunable transverse magnetic focusing in graphene *Nat. Phys.* **9** 225–9
[34] Wang R, Deacon R S, Car D, Bakkers E P A M and Ishibashi K 2016 InSb nanowire double quantum dots coupled to a superconducting microwave cavity *Appl. Phys. Lett.* **108** 203502
[35] Beenakker C W J and van Houten H 1991 Quantum transport in semiconductor nanostructures *Solid State Phys.* **44** 1–228
[36] Shin S K, Huang S Y, Fukata N and Ishibashi K 2012 Top-gated germanium nanowire quantum dots in a few-electron regime *Appl. Phys. Lett.* **100** 073103

[37] Lee P A and Stone A D 1985 universal conductance fluctuations in metals *Phys. Rev. Lett.* **55** 1622–5
[38] Hu J and Rosenbaum T F 2008 Classical and quantum routes to linear magnetoresistance *Nat. Mater.* **7** 697–700
[39] Parish M M and Littlewood P B 2003 Non-saturating magnetoresistance in heavily disordered semiconductors *Nature* **426** 162–5
[40] Tian J F, Chang C Z, Cao H L, He K, Ma X C, Xue Q K and Chen Y P 2014 Quantum and classical magnetoresistance in ambipolar topological insulator transistors with gate-tunable bulk and surface conduction *Sci. Rep.* **4** 4859
[41] Ning W, Du H F, Kong F Y, Yang J Y, Han Y Y, Tian M L and Zhang Y H 2013 One-dimensional weak antilocalization in single-crystal Bi_2Te_3 nanowires *Sci. Rep.* **3** 1564
[42] Beenakker C W J and van Houten H 1988 Boundary scattering and weak localization of electrons in a magnetic field *Phys. Rev.* B **38** 3232–40
[43] Cha J J, Claassen M, Kong D S, Hong S S, Koski K J, Qi X L and Cui Y 2012 Effects of magnetic doping on weak antilocalization in narrow Bi_2Se_3 nanoribbons *Nano Lett.* **12** 4355–9
[44] Lin J J and Bird J P 2002 Recent experimental studies of electron dephasing in metal and semiconductor mesoscopic structures *J. Phys. Condens. Matter* **14** R501
[45] Altshuler B L, Aronov A G and Khmelnitzky D E 1982 Effects of electron-electron collisions with small energy transfers on quantum localisation *J. Phys. C: Solid State Phys.* **15** 7367
[46] Yafet Y 1963 g Factors and spin-lattice relaxation of conduction electrons *Phys. Rev. B. Solid State* **14** 1–98
Elliott R J 1954 Theory of the effect of spin–orbit coupling on magnetic resonance in some semiconductors *Phys. Rev.* **96** 266–79
[47] D'yakonov M I and Perel' V I 1971 Spin orientation of electrons associated with the interband absorption of light in semiconductors *Sov. Phys. JETP* **33** 1053–9
[48] Golub L E and Ivchenko E L 2004 Spin splitting in symmetrical SiGe quantum well *Phys. Rev.* B **69** 115333
[49] Kunihashi Y, Kohda M and Nitta J 2009 Enhancement of spin lifetime in gate-fitted InGaAs narrow wires *Phys. Rev. Lett.* **102** 226601
[50] Kettemann S 2007 Dimensional control of antilocalization and spin relaxation in quantum wires *Phys. Rev. Lett.* **98** 176808